# Precision Υ spectroscopy from nonrelativistic lattice QCD

C. T. H. Davies,[1] K. Hornbostel,[2] A. Langnau,[3] G. P. Lepage,[3] A. Lidsey,[1] J. Shigemitsu,[4] and J. Sloan[5]

[1] *University of Glasgow, Glasgow, United Kingdom G12 8QQ*

[2] *Southern Methodist University, Dallas, Texas 75275*

[3] *Newman Laboratory of Nuclear Studies, Cornell University, Ithaca, New York 14853*

[4] *The Ohio State University, Columbus, Ohio 43210*

[5] *Supercomputer Computations Research Institute, Florida State University, Tallahassee, Florida 32306*

(Received 17 June 1994)

The spectrum of the Υ system is investigated using the nonrelativistic lattice QCD approach to heavy quarks and ignoring light quark vacuum polarization. We find good agreement with experiment for the Υ, Υ', Υ'' and for the center of mass and fine structure of the $\chi_b$ states. The lattice calculations predict $b\bar{b}$ D states with a center of mass at $(10.20 \pm 0.07 \pm 0.03)$ GeV. Fitting procedures aimed at extracting both ground and excited state energies are developed. We calculate a nonperturbative dispersion mass for the $\Upsilon(1S)$ and compare it with tadpole-improved lattice perturbation theory.

PACS number(s): 12.38.Gc, 12.39.Hg, 14.40.Gx, 14.65.Fy

## I. INTRODUCTION

Hadrons containing one or more heavy quarks have been the focus of intense investigations by lattice gauge theorists in recent years. One motivating factor is that these systems are also being studied extensively by experimentalists trying to nail down the remaining parameters in the standard model. Nonperturbative QCD results are needed in many instances to convert experimental numbers into determinations of fundamental parameters or to test the standard model. The lattice approach to nonperturbative QCD is now starting to yield reliable numbers for several of these crucial inputs. Part of the activity has been in heavy-light systems, focusing on leptonic and semileptonic decays of heavy-light mesons (the $B$'s and $D$'s) and on neutral meson mixing [1]. Another area of investigation, which is also the focus of the present article, has concentrated on heavy-heavy systems such as the $J/\psi$ and Υ families. Studies of the latter systems have already lead to the most accurate lattice determinations of the strong coupling constant $\alpha_s$ [2–4], and of the $b$-quark pole mass $M_b$ [5]. In heavy-heavy systems one can take advantage of the fact that only heavy quark propagators are required to do high statistics simulations at only modest computational cost (of course only once the gauge configurations have been created). This coupled with the wealth of experimental data on quarkonium allows one to carry out stringent tests of computational methods employed by lattice gauge theorists. These systems may also be the place where effects of quenching can be studied quantitatively. We report here on a study of the Υ system using the nonrelativistic QCD (NRQCD) [6,7] approach to heavy fermions. Our goal is to start from a first principles QCD Hamiltonian and show that it can reproduce the Υ spectrum. Along the way we develop and refine methods to analyze numerical data, methods that we hope will be useful in other lattice calculations as well. For instance, we find that extracting excited state energies is straightforward using our fitting procedures. Our simulations also serve to test perturbation theory on the lattice in a new setting, through comparisons of nonperturbative simulation results for the Υ kinetic mass with perturbative formulas. The investigations in this article provide the foundations for our determination of the $b$-quark pole mass. The $M_b$ calculations are described in a separate publication [5]. We emphasize that NRQCD provides an extremely efficient way to obtain realistic and accurate heavy quark propagators. The prospect of NRQCD having impact not only in investigations of heavy-heavy but also of heavy-light systems looks very promising [9].

The $b$ quarks in the Υ system are quite nonrelativistic, with $v^2 \sim 0.1$. The splittings between spin-averaged levels are around $\sim 500$ MeV $[O(M_b v^2)]$, which is much smaller than the mass $[O(2M_b)]$, indicating that a systematic expansion of the QCD Hamiltonian in powers of $v^2$ is very appropriate here. The continuum action density, correct through $O(M_b v^4)$, is given by

$$\mathcal{L}_{\text{cont}} = \psi^\dagger \left( D_t + H_0^{\text{cont}} \right) \psi + \psi^\dagger \, \delta H^{\text{cont}} \, \psi, \qquad (1)$$

with

$$H_0^{\text{cont}} = -\frac{\mathbf{D}^2}{2M_b^0},$$

$$\delta H^{\text{cont}} = -c_1 \frac{1}{8(M_b^0)^3} (\mathbf{D}^2)^2 + c_2 \frac{ig}{8(M_b^0)^2} (\mathbf{D} \cdot \mathbf{E} - \mathbf{E} \cdot \mathbf{D}) - c_3 \frac{g}{8(M_b^0)^2} \boldsymbol{\sigma} \cdot (\mathbf{D} \times \mathbf{E} - \mathbf{E} \times \mathbf{D}) - c_4 \frac{g}{2M_b^0} \boldsymbol{\sigma} \cdot \mathbf{B}. \qquad (2)$$

<u>50</u>          6963

$\psi$, $\psi^\dagger$ are two component Pauli spinors and at the tree level we have $c_i = 1$ for all $i$. Previous NRQCD studies [6,10] have used the leading order Hamiltonian ($\delta H = 0$) or the leading order plus the $\boldsymbol{\sigma} \cdot \mathbf{B}$ term and gave encouraging results. Here we include all the $O(M_b v^4)$ terms. This means systematic errors due to relativity will be of $O(M_b v^6) \sim 5$ MeV, which is about 1% of a typical radial or orbital excitation energy and 10% of a typical spin splitting.

In our lattice simulations there will be other sources of systematic errors. Finite volume errors are not a problem here since the $\Upsilon$'s are smaller than regular light hadrons. Finite lattice spacing errors in the fermionic action can be corrected for order by order, similar to the systematic $v^2$ corrections. This is explained in Ref. [7], where the relation to other improvement programs such as the Symanzik program [8] is also discussed. The main remaining sources of systematic errors come from the gauge configurations, namely, $O(a^2)$ errors from using the standard Wilson gauge action and quenching errors due to the absence of light quark vacuum polarization. From potential model calculations we estimate the latter errors to be the dominant ones. One consequence of quenching will be that inverse lattice spacings $a^{-1}$ extracted from different observables will not agree with each other in general, and one will have to make some choice when presenting dimensionful results. We find that our two basic splittings, the $1S$-$1P$ and the $1S$-$2S$ $\Upsilon$ energy level splittings, give $a^{-1}$'s that differ by one to two $\sigma$. We use an "average" lattice spacing in our dimensionful plots.

Finally, we need to discuss the number of parameters in the NRQCD action. In addition to the bare mass $M_b^0$ and the gauge coupling $g$ one has the $c_i$'s. We work with the $c_i$'s set to their tree-level values $c_i = 1$ while at the same time "tadpole improving" the lattice version of the NRQCD action [11]. This ensures an optimal perturbative scheme so that one can expect renormalization effects to be small. We find that, in practice, tree level values give the correct $P$-state fine structure splittings, giving us confidence that setting $c_i = 1$ is a viable approach. The final parameter we must consider is the zero of energy which is used to relate NRQCD energies with absolute, relativistic energies (this term is usually omitted from NRQCD actions). As with the $c_i$'s, it can be fixed at tree level to equal $M_b^0$, or calculated in perturbation theory. It can also be calculated nonperturbatively by requiring that the dispersion relation of the $\Upsilon$ be Lorentz invariant, up to the order in $v^2$ at which we are working. We find excellent agreement between perturbative and nonperturbative determinations, further encouraging us that perturbation theory is working. We stress that the only free parameters which we tune to match experimental results are those appearing in the original QCD action, $M_b^0$ and $g$. In other words, this is a first-principles QCD calculation, *not* a QCD-inspired phenomenological model. The coupling $g$ is eliminated as a free parameter, in the usual way, when we fix the scale $a^{-1} = a^{-1}(g)$ to match the $1S$ - $1P$ and/or the $1S$-$2S$ splitting. $M_b^0$ is tuned so that the simulated kinetic mass for the $\Upsilon$ agrees with the experimental $\Upsilon(1S)$ mass.

Our results for the spectrum of the $\Upsilon$ system are shown in Figs. 1 and 2. We use $a^{-1} = 2.4$ GeV, which is an average between the inverse lattice spacings obtained from the $\Upsilon$ $1S$-$2S$ and $1S$-$1P$ splittings (the error in this estimate for $a^{-1}$ is at the 4% level, details are given in Sec. IV). One sees that the general features of the known spectrum are reproduced nicely [12]. Figure 1 shows the $\Upsilon$, $\eta_b$, and singlet $P$ and $D$ states and Fig. 2 shows the $P$-state fine structure. In both figures the errors reflect statistical errors plus some systematic fitting errors. We do not show estimates of systematic errors due to quenching or the effects of uncertainties in the scale $a^{-1}$.

Both the $\eta_b$ and $D$ states (center of mass) are predictions of the theory. We find an $\eta_b$ state at $(9.431 \pm 0.005 \pm 0.001)$ GeV and $D$ states with a center of mass at $(10.20 \pm 0.07 \pm 0.03)$ GeV. These numbers include the dominant statistical and/or systematic errors other than those due to quenching. For the $D$ states the first error corresponds to the statistical error in fitting the $D$ mass in lattice units. For the $\eta_b$ state this error is negligible, and so the first error quoted there is the systematic error from neglected higher order relativistic terms and finite lattice spacing corrections. In both cases the second error arises from the uncertainty in the value of $a^{-1}$. We expect the $S$ states and hence also the $\Upsilon$-$\eta_b$ splitting to have noticeable quenching errors. Spectrum calculations with dynamical gauge configurations are already underway. It will be interesting to compare the quenched and unquenched spectra.

In the rest of the article we give more details of our analyses, starting with the quark propagator calculations and the meson correlations in the next section. Section III includes a lengthy explanation of our fitting procedures. The main message there is that, instead of going to large time slices in search of a plateau, we have worked with high statistics correlations on shorter lattices (24 time slices) and carried out simultaneous multi-exponential fits to several correlations at a time. We also
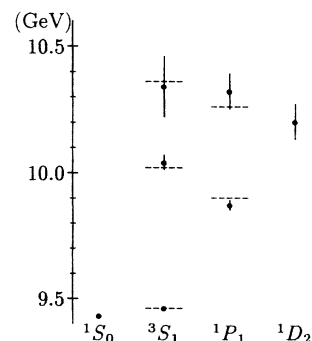


FIG. 1. NRQCD simulation results for the spectrum of the $\Upsilon$ system including radial excitations. Experimental values (dashed lines) are indicated for the triplet $S$ states, and for the spin-average of the triplet $P$ states. The energy zero from simulation results is adjusted to give the correct mass to the $\Upsilon(1^3S_1)$.
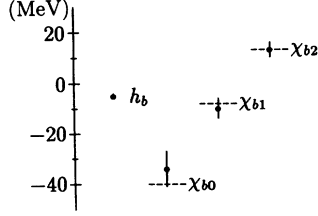
FIG. 2. Simulation results for the spin structure of the lowest lying $P$-wave states in the $\Upsilon$ family. The dashed lines are the experimental values for the triplet states. Energies are measured relative to the center of mass of the triplet states.

devised methods to extract splittings directly. Our statistical errors for spin-averaged level splittings are about 20–30 MeV, for $P$-state fine structure splittings about 5–10 MeV and for the $S$-state spin splitting down to 0.5 MeV. In Sec. IV we discuss determination of $a^{-1}$ and comparison with experiment. We also present results for meson wave functions at the origin. Section V describes the extraction of a "kinetic mass" $aM_{\rm kin}$, for the $\Upsilon(1S)$ from correlations with momenta and comparisons with perturbation theory. Section VI gives a brief summary.

## II. THE SIMULATION

### A. Quark propagators

Quark propagators in lattice NRQCD are determined, in a single pass through the gauge-field configuration, from evolution equations that specify the propagator for $t > 0$ in terms of its value at $t = 0$. Various evolution equations have been suggested in the past. Currently we use the equation proposed in [7], modified slightly for improved efficiency. Our propagators are defined by the equation

$$\left(1-\frac{aH_0}{2n}\right)^{-n} U_4 \left(1-\frac{aH_0}{2n}\right)^{-n} G_{t+1} - (1-a\,\delta H)\,G_t$$
$$= \delta_{\mathbf{x},0}\,\delta_{t,0}, \quad (3)$$

where $G_t = 0$ for $t \leq 0$. For numerical work it is convenient to rewrite this equation in the form

$$G_1 = \left(1-\frac{aH_0}{2n}\right)^n U_4^\dagger \left(1-\frac{aH_0}{2n}\right)^n \delta_{\mathbf{x},0},$$

$$G_{t+1} = \left(1-\frac{aH_0}{2n}\right)^n U_4^\dagger \left(1-\frac{aH_0}{2n}\right)^n (1-a\delta H)\,G_t$$

$$(t > 0). \quad (4)$$

On the lattice, the kinetic energy operator is

$$H_0 = -\frac{\Delta^{(2)}}{2M_b^0}, \quad (5)$$

and the correction terms are

$$\delta H = -c_1 \frac{(\Delta^{(2)})^2}{8(M_b^0)^3} + c_2 \frac{ig}{8(M_b^0)^2} (\mathbf{\Delta}\cdot\mathbf{E} - \mathbf{E}\cdot\mathbf{\Delta})$$
$$-c_3 \frac{g}{8(M_b^0)^2}\boldsymbol{\sigma}\cdot(\mathbf{\Delta}\times\mathbf{E} - \mathbf{E}\times\mathbf{\Delta}) - c_4 \frac{g}{2M_b^0}\,\boldsymbol{\sigma}\cdot\mathbf{B}$$
$$+c_5 \frac{a^2\Delta^{(4)}}{24M_b^0} - c_6 \frac{a(\Delta^{(2)})^2}{16n(M_b^0)^2}. \quad (6)$$

The last two terms in $\delta H$ come from finite lattice spacing corrections to the lattice Laplacian and the lattice time derivative, respectively. $\mathbf{\Delta}$ is the symmetric lattice derivative and $\Delta^{(4)}$ is a lattice version of the continuum operator $\sum D_i^4$. We used the standard cloverleaf operators for the chromoelectric and magnetic fields $\mathbf{E}$ and $\mathbf{B}$. The parameter $n$ is introduced to remove instabilities in the heavy quark propagator caused by the highest momentum modes of the theory. For our simulations at $\beta = 6.0$ and with bare masses relevant for the $\Upsilon$ system, we set $n = 2$.

As mentioned in the Introduction, we tadpole-improve our lattice action by dividing all the $U$'s that appear in $\mathbf{E}$, $\mathbf{B}$, and the covariant lattice derivatives fields by $u_0$, the fourth root of the plaquette [11]. This is most easily done as the $U_\mu$'s are read by the simulation code. The effect is to transform the operators that appear in the evolution Eqs. (4) as follows:

$$U_4^\dagger \longrightarrow U_4^\dagger/u_0, \quad (7)$$

$$\mathbf{E} \longrightarrow \mathbf{E}/(u_0)^4, \quad (8)$$

$$\mathbf{B} \longrightarrow \mathbf{B}/(u_0)^4, \quad (9)$$

$$\Delta_\mu G(x) \longrightarrow [U_\mu(x)G(x+\hat{\mu})$$
$$-U_\mu^\dagger(x-\hat{\mu})G(x-\hat{\mu})]/2u_0, \quad (10)$$

$$\Delta_\mu^{(2)} G(x) \longrightarrow [U_\mu(x)G(x+\hat{\mu})$$
$$+U_\mu^\dagger(x-\hat{\mu})G(x-\hat{\mu})]/u_0 - 2G(x), \quad (11)$$

with

$$\Delta^{(2)} = \sum_\mu \Delta_\mu^{(2)}, \quad (12)$$

$$\Delta^{(4)} = \sum_\mu (\Delta_\mu^{(2)})^2. \quad (13)$$

Tadpole improvement of the action allows us to work with tree-level values for the $c_i$'s in $\delta H$ without having to worry about large renormalizations. Hence our lattice action depends only on two parameters: the bare mass $M_b^0$ and the QCD coupling constant $g$. We have collected data for three values of the bare mass, $aM_b^0 = 1.71$, 1.8, and 2.0, all at $\beta = 6.0$. For this $\beta$, $u_0 = 0.878$.

We computed our quark propagators for $aM_b^0 = 1.8$, 2.0 using a different evolution equation:

$$U_4\,G_{t+1} - \left(1-\frac{aH_0}{2n}\right)^n (1-a\delta H)\left(1-\frac{aH_0}{2n}\right)^n G_t$$

$$= \delta_{\mathbf{x},0}\,\delta_{t,0}. \quad (14)$$

Propagators from this evolution equation are the same as those from the other equation [Eq. (3)], but with extra factors of $(1 - aH_0/2n)^{-n}$ in both the source and sink. These extra factors cannot affect the meson spectrum, but they do modify the quark's wave function normalization to order $v^2$. For this reason our other formulation [Eq. (3)] is superior; with it, NRQCD quark fields are normalized to unity up to corrections of order $\alpha_s$ and $v^4$.

## B. Meson correlation functions

Once one has the quark propagators it is straightforward to obtain meson propagators. Let $\psi^\dagger$ and $\chi^\dagger$ denote fields that create a heavy quark or heavy antiquark, respectively. The following interpolating operator creates a meson of momentum $\mathbf{p}$, where it is understood that we are working in a fixed (Coulomb) gauge:

$$\sum_{\mathbf{x}_1,\mathbf{x}_2} \psi^\dagger(\mathbf{x}_1) \, \Gamma(\mathbf{x}_1 - \mathbf{x}_2) \, \chi^\dagger(\mathbf{x}_2) \, e^{i\frac{\mathbf{p}}{2}\cdot(\mathbf{x}_1+\mathbf{x}_2)}. \tag{15}$$

The "meson operator" $\Gamma$ can be written as $\Gamma(\mathbf{x}_1 - \mathbf{x}_2) = \Omega \, \phi(|\mathbf{x}_1 - \mathbf{x}_2|)$. The operator $\Omega$ is a $2 \times 2$ matrix in

spin space and generally includes derivatives acting on the radial function $\phi(r)$. Using translation invariance, we eliminate the summation over the initial antiquark position. The meson propagator is then

$$G_{\text{meson}}(\mathbf{p}, t) = \sum_{\mathbf{y}_1,\mathbf{y}_2} \text{Tr}\left[ G_t^\dagger(\mathbf{y}_2) \, \Gamma^{(\text{sk})\dagger}(\mathbf{y}_1 - \mathbf{y}_2) \tilde{G}_t(\mathbf{y}_1) \right]$$
$$\times e^{-i\frac{\mathbf{p}}{2}\cdot(\mathbf{y}_1+\mathbf{y}_2)}, \tag{16}$$

with

$$\tilde{G}_t(\mathbf{y}) \equiv \sum_{\mathbf{x}} G_t(\mathbf{y} - \mathbf{x}) \, \Gamma^{(\text{sc})}(\mathbf{x}) e^{i\frac{\mathbf{p}}{2}\cdot\mathbf{x}}, \tag{17}$$

and the trace is over spin and color. In the above equations we distinguish between $\Gamma^{(\text{sc})}$ and $\Gamma^{(\text{sk})}$, i.e., the smearing at the source or sink. $\tilde{G}_t(\mathbf{x})$ can be obtained directly using Eq. (4) with $\delta_{\mathbf{x},0} \to \Gamma^{(\text{sc})}(\mathbf{x}) \, e^{i\frac{\mathbf{p}}{2}\cdot\mathbf{x}}$. In the future we will often refer to the smeared propagator $\tilde{G}$ as the quark propagator. The convolution in Eq. (16) is evaluated using fast-Fourier transforms.

In Table I we list the zero momentum $b\bar{b}$ meson states

TABLE I. Meson operators. $\Delta_i$ denotes the symmetric lattice derivative and $D_{ij} \equiv \Delta_i\Delta_j - \delta_{ij}\Delta^2/3$.

| Meson $^{2S+1}L_J$ $(J^{PC})$ | Lattice Rep. | $\Gamma = \Omega\phi(r)$ $\Omega$ | $\phi$ |
|---|---|---|---|
| $^1S_0$ $(0^{-+})$ | $A_1^{-+}$ | $\hat{I}$ | $\phi_{n_{\text{sc}}}^{(S)}(r)$; $\quad n_{\text{sc}} = \text{loc},1,2,3$ |
| $^3S_1$ $(1^{--})$ | $T_{1(i)}^{--}$ | $\sigma_i$ | |
| $^1P_1$ $(1^{+-})$ | $T_{1(i)}^{+-}$ | $\Delta_i$ | $\phi_{n_{\text{sc}}}^{(P)}(r)$; $\quad n_{\text{sc}} = \text{loc},1,2$ |
| $^3P_0$ $(0^{++})$ | $A_1^{++}$ | $\sum_j \Delta_j\sigma_j$ | |
| $^3P_1$ $(1^{++})$ | $T_{1(k)}^{++}$ | $\Delta_i\sigma_j - \Delta_j\sigma_i$ | |
| $^3P_2$ $(2^{++})$ | $E_{(k)}^{++}$ | $\Delta_i\sigma_i - \Delta_j\sigma_j$ | |
| | $T_{2(ij)}^{++}$ | $\Delta_i\sigma_j + \Delta_j\sigma_i$ $(i \neq j)$ | |
| $^1D_2$ $(2^{-+})$ | $E_{(k)}^{-+}$ | $D_{ii} - D_{jj}$ | $\phi_{n_{\text{sc}}}^{(D)}(r)$; $\quad n_{\text{sc}} = \text{loc},1,2$ |
| | $T_{2(ij)}^{-+}$ | $D_{ij}$ $(i \neq j)$ | |
| $^3D_1$ $(1^{--})$ | $T_{1(i)}^{--}$ | $\sum_j D_{ij}\sigma_j$ | |
| $^3D_2$ $(2^{--})$ | $E_{(j)}^{--}$ | $D_{ij}\sigma_k - D_{jk}\sigma_i$ | |
| | $T_{2(ij)}^{--}$ | $(D_{ii} - D_{jj})\sigma_k$ $+D_{jk}\sigma_j - D_{ki}\sigma_i$ | |
| $^3D_3$ $(3^{--})$ | $A_2^{--}$ | $(D_{ij}\sigma_k + D_{jk}\sigma_i + D_{ki}\sigma_j)/3$ | |
| | $T_{1(i)}^{--}$ | $D_{ii}\sigma_i - 2/5 \sum_j D_{ij}\sigma_j$ | |
| | $T_{2(ij)}^{--}$ | $(D_{ii} - D_{jj})\sigma_k$ $+2(D_{ki}\sigma_i - D_{kj}\sigma_j)$ | |

studied in the current project together with their corresponding meson operators, $\Gamma(\mathbf{x})$. We choose $\phi_{n_{sc}}(r)$ for $n_{sc} = 1, 2, 3$ to correspond to Richardson potential radial wave functions for the $S$-, $P$- or $D$-state ground and excited levels. We also used $\delta$-function local sources and sinks. These are referred to as $n_{sc} = $loc in Table I. For each set of meson quantum numbers we evaluated correlations with all possible independent smearings, $(n_{sc}, n_{sk}) = (\text{loc}, \text{loc}), (\text{loc}, 1), (\text{loc}, 2), ...$ at the source and the sink. So for the $S$ states we obtained a $4 \times 4$ matrix of correlation functions and for the $P$ and $D$ states $3 \times 3$ matrices. In addition we looked at $S$-state mesons with small momenta. For those we used $\phi_{\text{loc}}$ and $\phi_1$.

Table I also lists the continuum quantum numbers $J^{PC}$ and the lattice cubic group representations for our meson states. This allows us to see which states are expected to mix with each other. Mixing will occur both due to relativistic corrections and due to lattice artifacts. For instance, since $L$ is no longer a good quantum number in a relativistic theory the $^3S_1$ and the $^3D_1$ states will mix, both being $J^{PC} = 1^{--}$. This mixing, which happens even in the continuum limit, is suppressed by $v^2$. On the lattice one can also have mixing between different $J$ states that fall into the same lattice representations. Examples are mixing between $^3D_3T_2$ and $^3D_2T_2$ or between $^3D_3T_1$, $^3D_1T_1$, and $^3S_1$. We have measured cross correlations between these states, but postpone their analysis for future work, concentrating here on the spin-averaged $D$ states.

In the expression Eq. (15) one has sums over color and spin degrees of freedom. One could calculate quark (and antiquark) propagators separately for each color and spin quantum number at the source. We have done so for the color degrees of freedom and verify a reduction of statistical errors by $\sqrt{3}$ compared to when only one value for the initial quark and antiquark color was used. As far as spin is concerned we decided to save on CPU time by setting the initial quark and antiquark spins equal to 1. This means that at the source we are sensitive only to the 1-1 component of the $2 \times 2$ spin matrix in $\Gamma^{(sc)}$ and mesons of definite quantum numbers are projected out at the sink. From Table I one sees that groups of mesons such as $^1S_0$ and $^3S_1z$ , or $^1P_1x$ , $^3P_1y$, and $^3P_2T_2zx$ etc. have the same 1-1 component of $\Gamma^{(sc)}$ up to normalization. For each group, the meson correlations for its members can be obtained from one common quark propagator (this must be repeated for each smearing function, $\phi_{n_{sc}}$ at the source), and are highly correlated. We have taken advantage of these strong correlations to reduce statistical errors in our fits for hyperfine and fine structure splittings. We worked with 13 zero momentum quark propagators with $S$- or $P$-state smearing at the source and four $S$-state propagators with momentum. Out of these quark propagators 129 $S$- and $P$-state meson correlations were evaluated using different $\Gamma^{(sk)}$ and many combinations of smearing functions at source and sink. For $aM_b^0 = 1.71$ we also evaluated an additional 15 quark propagators with $D$-state smearing. To date we have only analyzed combinations of these $D$-state quark propagators giving rise to the $^1D_2$ mesons. With

five polarization and nine different source-sink smearing combinations, this means a total of 45 $D$-state meson correlations.

## III. DATA ANALYSIS AND FITTING RESULTS

Our calculations used $\beta = 6.0$ quenched gauge field configurations on $16^3 \times 24$ lattices provided by Greg Kilcup and his collaborators. We worked with an ensemble of 105 independent configurations that were gauge-fixed to Coulomb gauge. For each configuration we selected eight different origins on the first time slice for our quark (antiquark) propagators. Because of the small size of Υ mesons one expects to have negligible correlations among propagators from different origins, and this was confirmed by some simple tests. For instance, after binning over origins, errors in the correlation functions changed by at most 5% and essentially no changes were observed in $\chi^2$ values or in the errors and central values of fitted energies and amplitudes. For our $aM_b^0 = 1.71$ $P$ states we also ran with eight origins on time slice 12. This data was binned together with the time slice 1 data for each configuration and spatial origin. Hence for each of the 129 (or 129 + 45) meson correlations, discussed above, we worked with $105 \times 8 = 840$ measurements. In Figs. 3 and 4 we show some examples of effective mass plots for our data. The errors are bootstrap errors. Figure 3 shows $aM_b^0 = 1.8$ data for $^1S_0$ states. The effective mass plots are arranged as a $3 \times 3$ matrix corresponding to the nine source-sink combinations $(n_{sc}, n_{sk})$ with $n_{sc}, n_{sk} = $loc$, 1, 2$. Figure 4 shows similar plots for $aM_b^0 = 1.71$ $^1P_1$ data. We have averaged over $^1P_1x$, $^1P_1y$, and $^1P_1z$. This $h_b$ state has not been observed yet experimentally, but there are strong theoretical reasons for believing that it lies close to the center of mass of the $^3P$ levels. Hence we will sometimes refer to the $^1P_1$ level as the "spin averaged" $P$ state. One sees from Figs. 3 and 4 that our $S$-state correlations with $n_{sk} = $loc and $n_{sk} = 1$ sinks have excellent statistics. The $S$-state correlations with excited state smearing $n_{sk} = 2, 3$ and the $P$-state data have good to reasonable statistics. In the effective mass plots, truncations at large $t$ means that signal to noise in the original data was worse than $3:1$ beyond that point or that the correlation had switched sign. We have used the naive definition $m_{\text{eff}}(t) = \ln[G(t)/G(t+1)]$, although a more sophisticated version could be used when one deals with off-diagonal correlations in which some amplitudes can come in with negative signs. Our plots provide a rough assessment of the quality of the data; we do not use them in our fits.

### A. Fitting procedures for $^3S_1$ and singlet $P$ and $D$ states

We investigated a variety of fitting procedures to extract the spectrum from the meson correlations. For the $S$ states and singlet $P$ and $D$ states we used simultaneous multiexponential fits to several correlations in order to
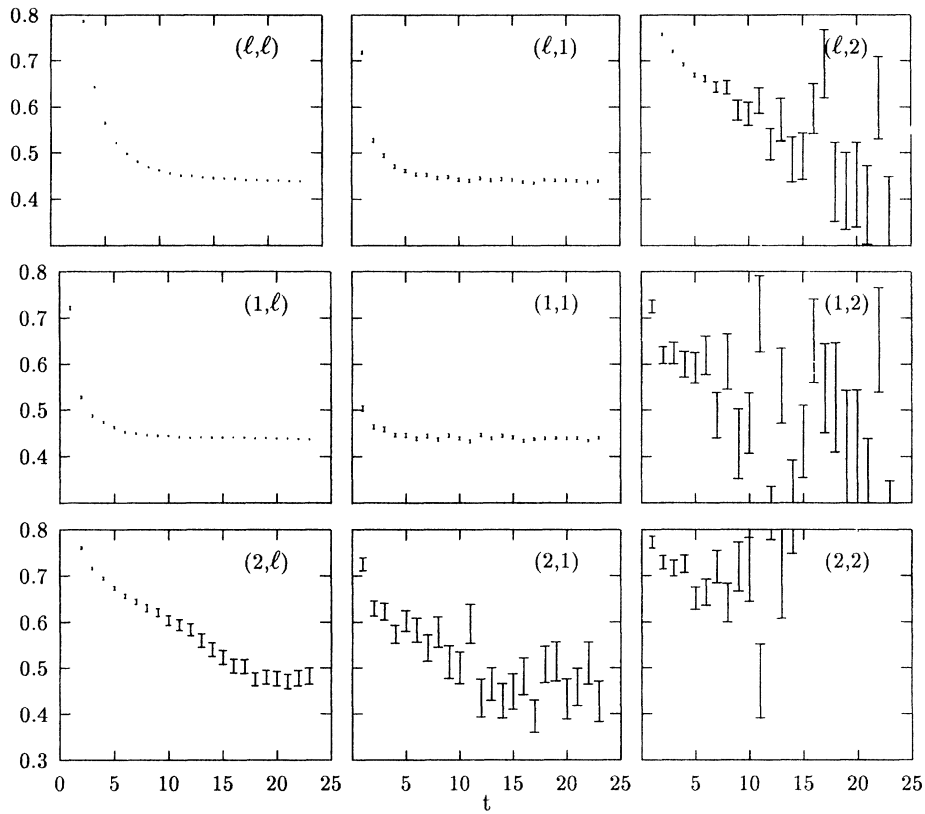
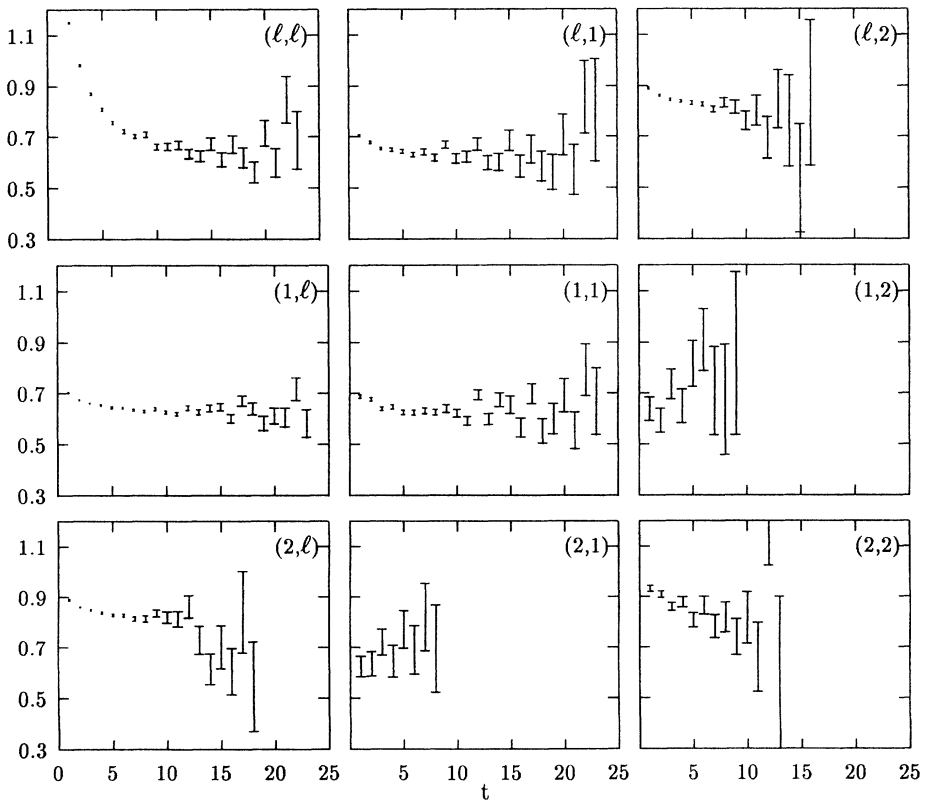FIG. 3. $^1S_0$ effective masses by (source, sink).



FIG. 4. $^1P_1$ effective masses by (source, sink).

obtain the ground state and one or two excited state energies. We employed mainly two such fitting procedures and got consistent results from both of them within one $\sigma$. In the first procedure, we fit simultaneously to a matrix of correlations with $n_{sc}, n_{sk} = 1, 2, 3$ for $S$ states and $n_{sc}, n_{sk} = 1, 2$ for the spin singlet $P$ and $D$ states. Similar fitting methods have been discussed by other groups in the past [13]. In the matrix fits each meson correlation is fit to the expression

$$G_{\text{meson}}(n_{sc}, n_{sk}; t) = \sum_{k=1}^{N_{\text{exp}}} a(n_{sc}, k) \, a^*(n_{sk}, k) \, e^{-E_k \cdot t}.$$

(18)

Using charge conjugation symmetry one can argue that, for equal mass quarks, the coefficients $a(j, k)$ can be chosen to be real numbers. From the effective mass plots of Figs. 3 and 4 it is clear that if one wants to make use of most of the data one does not want to move too far out with $t_{\text{min}}$ in search of a plateau. One wants instead to fit to several exponentials working with as small a $t_{\text{min}}$ value as possible while still maintaining good $\chi^2$'s. Multiexponential fits to a single correlation, however are usually tricky and unstable. It is much easier to do multiexponential fits to several correlations simultanously, especially if one makes sure that each exponential has a significant amplitude in at least one correlation. Although the number of parameters in our fits was sometimes large (we were typically doing 6-,9-,12-, and 16-parameter fits) they were highly constrained, and we did not run into stability problems. Since we had a large number, 840, of measurements to play with we also did not have to worry about the size of the covariance matrix becoming too large. We used $N_{\text{exp}} = 3$ for the $3 \times 3$ matrix fits and $N_{\text{exp}} = 2$ for the $2 \times 2$ matrix fits.

The second procedure for doing multicorrelation multi-exponential fits was to take a set of smeared-local correlations, $(n_{sc}, n_{sk}) = (n_{sc}, \text{loc})$ with $n_{sc} = 1, 2, 3$ or $n_{sc} = 1, 2$ and fit them simultaneously to the same set of energies, $E_k$. These smeared-local correlations have the smallest statistical errors. They are fit to

$$G_{\text{meson}}(n_{sc}, \text{loc}; t) = \sum_{k=1}^{N_{\text{exp}}} b(n_{sc}, k) \, e^{-E_k \cdot t}.$$

(19)

Note that this is the same ansatz as Eq. (18), with $b(n_{sc}, k) = a(n_{sc}, k) a^*(\text{loc}, k)$. We used $N_{\text{exp}} = 2$ or 3 when fitting two correlations and $N_{\text{exp}} = 3$ or 4 for three correlations. We use different sets of correlations for fitting procedures 1 and 2. So the fact that, as we will see, consistent energies are obtained from the two procedures gives us confidence in the final results.

In fitting correlations the delicate question is always how to pick the range $t_{\text{min}}/t_{\text{max}}$ in $t$ over which to fit. Needless to say, in our multiexponential fits the larger $N_{\text{exp}}$, the smaller we can make $t_{\text{min}}$. On the other hand for fixed $N_{\text{exp}}$ when one increases $t_{\text{min}}$ there could come a point when the signal for the higher exponential is no longer above the noise leading to larger errors in the energies of even the lower lying levels. To illustrate some of these issues we show in Table II examples of fits to $aM_b^0 = 1.71$ ${}^3S_1$ states using procedure 2. We tabulate results for different number of exponentials and correlations and show the dependence on $t_{\text{min}}/t_{\text{max}}$. The last column gives $Q$, the "goodness of fit", i.e., the probability that fluctuations in correctly modeled data will generate a $\chi^2$ greater than that of the fit. One usually desires $Q > 0.1$, but slightly smaller values do not necessarily rule out a fit. Table II starts with two exponential fits to two correlations with $(n_{sc}, n_{sk}) = (1, \text{loc})$ and $(2, \text{loc})$. One sees that for $t_{\text{min}}$ of 6 to 8 good fits are obtained to the ground and first excited level. For $t_{\text{min}} = 4$ the $Q$

TABLE II. Examples of simultaneous multiexponential fits to two and three ${}^3S_1$ smeared-local correlations.

| | $N_{\text{exp}}$ | $t_{\text{min}}/t_{\text{max}}$ | $aE_1$ | $aE_2$ | $aE_3$ | $Q$ |
|---|---|---|---|---|---|---|
| Fits to (1,loc ) | 2 | 8/24 | 0.4533(8) | 0.707(9) | | 0.62 |
| and (2,loc) | | 7/24 | 0.4531(8) | 0.702(8) | | 0.63 |
| | | 6/24 | 0.4531(7) | 0.707(6) | | 0.68 |
| | | 5/24 | 0.4533(7) | 0.712(5) | | 0.62 |
| | | 4/24 | 0.4533(7) | 0.725(5) | | 0.04 |
| | | 3/24 | 0.4537(7) | 0.740(4) | | $7 \times 10^{-5}$ |
| | 3 | 5/24 | 0.4531(8) | 0.70(2) | 1.0(6) | 0.57 |
| | | 4/24 | 0.4534(8) | 0.69(1) | 1.1(2) | 0.54 |
| | | 3/24 | 0.4531(4) | 0.69(1) | 1.1(1) | 0.48 |
| | | 2/24 | 0.4531(7) | 0.69(1) | 1.0(1) | 0.45 |
| Fits to (1,loc), | 3 | 7/24 | 0.4533(9) | 0.72(3) | 0.82(5) | 0.76 |
| (2,loc), (3,loc) | | 6/24 | 0.4533(9) | 0.72(5) | 0.83(8) | 0.77 |
| | | 5/24 | 0.4530(8) | 0.71(7) | 0.85(9) | 0.75 |
| | | 4/24 | 0.4535(8) | 0.68(1) | 0.91(2) | 0.64 |
| | | 3/24 | 0.4531(8) | 0.69(1) | 0.95(1) | 0.33 |
| | 4 | 4/24 | 0.4529(9) | 0.71(4) | 0.82(10) | 0.74 |
| | | 3/24 | 0.4530(8) | 0.71(2) | 0.80(2) | 0.51 |

TABLE III. Examples of $2 \times 2$ and $3 \times 3$ matrix fits to $^3S_1$ correlations.

| | $N_{exp}$ | $t_{min}/t_{max}$ | $aE_1$ | $aE_2$ | $aE_3$ | $Q$ |
|---|---|---|---|---|---|---|
| Fits to | 2 | 5/24 | 0.4537(7) | 0.694(7) | | 0.10 |
| (1,1), (1,2) | | 5/22 | 0.4539(7) | 0.693(7) | | 0.17 |
| (2,1), (2,2) | | 6/24 | 0.4536(7) | 0.708(9) | | 0.24 |
| | | 6/22 | 0.4538(7) | 0.708(9) | | 0.41 |
| | | 6/16 | 0.455(1) | 0.71(1) | | 0.21 |
| | | 7/24 | 0.4536(7) | 0.70(1) | | 0.17 |
| | | 7/22 | 0.4539(7) | 0.70(1) | | 0.31 |
| | | 8/24 | 0.4534(7) | 0.71(1) | | 0.13 |
| | | 8/22 | 0.4537(8) | 0.71(1) | | 0.24 |
| Fits to | 3 | 4/24 | 0.4540(6) | 0.702(6) | 0.88(2) | 0.04 |
| (1,1), (1,2) | | 5/24 | 0.4538(6) | 0.697(8) | 0.86(3) | 0.06 |
| (2,1), (2,2) | | 5/22 | 0.4540(7) | 0.696(8) | 0.86(3) | 0.06 |
| (1,3), (3,1) | | 6/24 | 0.4536(7) | 0.710(9) | 0.90(7) | 0.14 |
| (2,3), (3,2) | | 6/22 | 0.4538(7) | 0.709(9) | 0.89(7) | 0.18 |
| (3,3) | | 6/16 | 0.455(1) | 0.711(9) | 0.90(9) | 0.05 |
| | | 7/24 | 0.4537(7) | 0.67(3) | 0.74(2) | 0.22 |
| | | 7/22 | 0.4540(7) | 0.67(3) | 0.74(2) | 0.31 |
| | | 8/24 | 0.4534(7) | 0.64(5) | 0.724(9) | 0.49 |

value starts to deteriorate. Adding a third exponential allows one to go down to $t_{min}$ of 2. The third energy $E_3$, however, is not reliable yet until we include another correlation with $\phi_3$ smearing. Such fits, i.e., simultaneous fits to three correlations, $G_{^3S_1}(1,\mathrm{loc};t)$, $G_{^3S_1}(2,\mathrm{loc};t)$ and $G_{^3S_1}(3,\mathrm{loc};t)$ are also shown in Table II.

In Table III we give examples of $2 \times 2$ and $3 \times 3$ matrix fits (procedure 1) to $^3S_1$ levels for several $t_{min}/t_{max}$. The results are consistent with Table II but with generally worse $Q$ values. For the $3 \times 3$ matrix fits one sees that the signal for the second excited state has disappeared once $t_{min} > 6$. The errors in Tables II and III are obtained by the criterion that $\delta\chi^2 = 1$. We have checked that bootstrap errors agree with these errors to within ±10%. This indicates that the statistical fluctuations in our correlations are close to being Gaussian. In Figs. 5 and 6 we show "effective amplitude" plots (for $G_{meson}(t)\,e^{E_1 \cdot t}$) corresponding to the $N_{exp} = 3$, $t_{min}/t_{max} = 5/24$ fit to two correlations in Table II and the $3 \times 3$ matrix fit with $t_{min}/t_{max} = 7/22$ in Table III. One sees that most of the correlations are reproduced reasonably well by our fits.

Information on how well our smearing functions are doing is contained in the fitted amplitudes, the $a(n,k)$'s and $b(n,k)$'s of Eq. (18) and Eq. (19). These measure

the overlap between our smearing functions and energy eigenstate wave functions. In Table IV we show $a(n,k)$ for several matrix fits of Table III and similarly in Table V we show $b(n,k)$ of smeared-local fits. One sees for instance that with $n_{sc,sk} = 1$, the amplitude for the ground state ($k = 1$) dominates, whereas for $n_{sc,sk} = 2$ or $n_{sc,sk} = 3$ one has the largest overlap with, respectively, the first or second excited state ($k = 2$ or $k = 3$). Our Richardson potential smearing functions are doing a reasonable job in focusing correlations onto the right levels. One might do better by using our own simulations to provide good smearing functions. We are planning to do this in future simulations.

The multicorrelation multiexponential fits described above were used to obtain energies for the $\eta_b$, $\Upsilon$, the $h_b$ levels, and the singlet $D$ states. The $\eta_b$ fits are similar to those shown for $\Upsilon$ states. The $h_b$ and the $D$-state correlations are more noisy. We give examples of fits for the $h_b$ levels in Table VI using $2 \times 2$ matrix fits [with $(n_{sc}, n_{sk}) = (1,1),(1,2),(2,1),$ and $(2,2)$] and using simultaneous fits to $(n_{sc}, n_{sk}) = (1,\mathrm{loc})$ and $(2,\mathrm{loc})$. We will give summaries of all our fits for different $M_b^0$ below, where we also convert dimensionless numbers into real energies in GeV. Here we go on to describe fitting procedures used
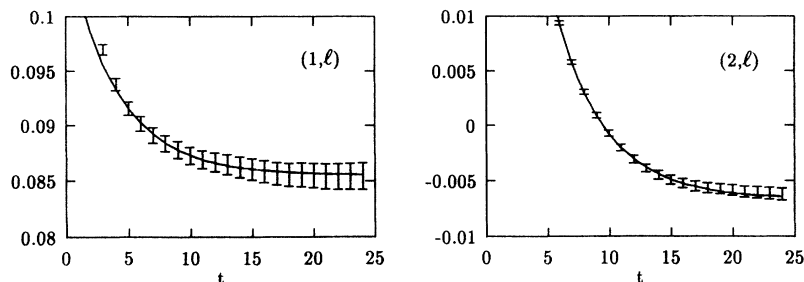


FIG. 5. $^3S_1$ effective amplitudes $G(t)e^{E_1 \cdot t}$ from three-exponential fits with $t_{min} = 5$, $t_{max} = 24$.

TABLE IV. Examples of fit results for amplitudes $a(n_{sc,sk}, k)$.

| Fit | $t_{min}/t_{max}$ | $k$ | $a(n_{sc,sk} = 1, k)$ | $a(n_{sc,sk} = 2, k)$ | $a(n_{sc,sk} = 3, k)$ |
|---|---|---|---|---|---|
| $N_{exp} = 2$ fits to | 6/22 | 1 | 0.877(5) | -0.065(3) | |
| (1,1), (2,2) | | 2 | 0.18(1) | 0.79(3) | |
| (1,2), (2,1) | 7/22 | 1 | 0.878(5) | -0.066(3) | |
| | | 2 | 0.18(2) | 0.78(3) | |
| $N_{exp} = 3$ fits to | 6/22 | 1 | 0.877(5) | -0.065(3) | -0.015(1) |
| (1,1), (1,2), (2,1) | | 2 | 0.18(1) | 0.79(2) | 0.07(4) |
| (1,3), (3,1), (2,2) | | 3 | 0.094(9) | -0.1(1) | 0.8(2) |
| (3,3) | 5/22 | 1 | 0.878(4) | -0.066(3) | -0.014(1) |
| | | 2 | 0.17(1) | 0.75(2) | 0.03(4) |
| | | 3 | 0.09(1) | 0.09(8) | 0.70(6) |

to obtain fine-structure splittings between the $\chi_b$ states, the $\Upsilon$-$\eta_b$ splitting, and the splitting between states with zero and nonzero momenta.

## B. Fitting procedures for spin splittings

One test of the NRQCD effective action is to see how well the fine and hyperfine structure in the $b\bar{b}$ system can be reproduced. These splittings will be the ones most sensitive to the coefficients $c_i$ in the action and the question is whether, with tadpole-improvement, tree-level values of $c_i = 1$ are adequate. The splittings between the

$\chi_b$ states are a few tens of MeV. From Table VI one sees that direct determination of $P$-state levels have errors that are at best 0.005–0.010 in dimensionless units. With an inverse lattice spacing of $a^{-1} \simeq 2.4$ GeV (see next section) this corresponds to an error of 12 to 24 MeV, and it seems marginal whether we would be able to resolve fine structure if each $P$ level were fit independently. To get around this problem one can take advantage of the fact that correlation functions for different mesons on the same configuration can be highly correlated. This allows for a direct fit to the mass splitting between them. We have employed two methods for extracting splittings: $\delta E = E_1^A - E_1^B$, from two very corre-
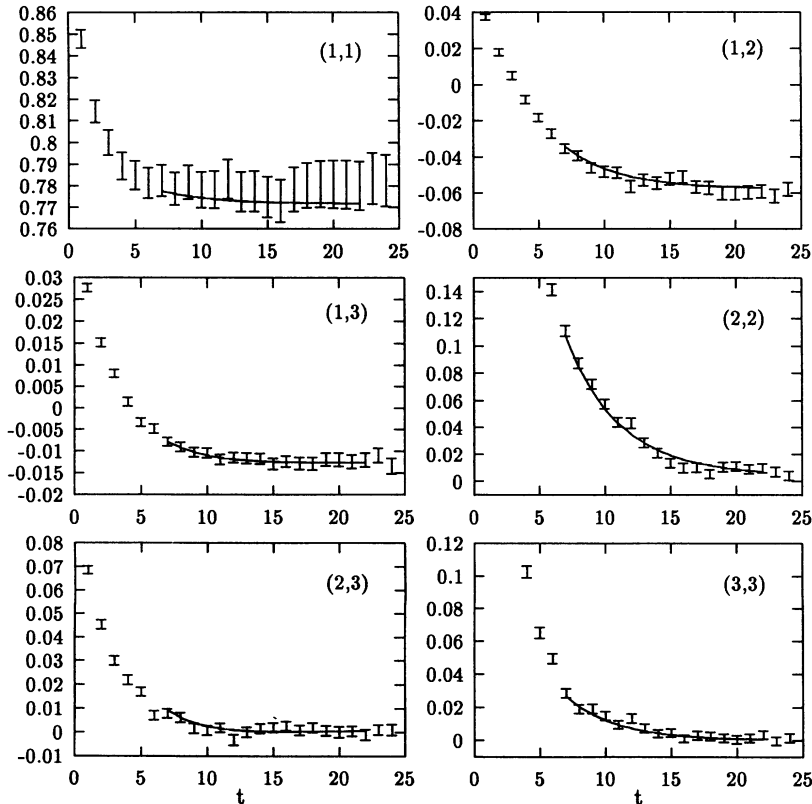


FIG. 6. $^3S_1$ effective amplitudes $G(t)e^{E_1 \cdot t}$ for three by three matrix fits with $t_{min} = 7$, $t_{max} = 22$. Off-diagonal fits are averaged over source and sink.

TABLE V. Examples of fit results for amplitudes $b(n_{sc}, k)$.

| Fit | $t_{min}/t_{max}$ | $k$ | $b(n_{sc} = 1, k)$ | $b(n_{sc} = 2, k)$ | $b(n_{sc} = 3, k)$ |
|---|---|---|---|---|---|
| $N_{exp} = 2$ fits to | 6/24 | 1 | 0.135(2) | -0.0102(8) | |
| (1,loc) and (2,loc) | | 2 | 0.032(4) | 0.114(2) | |
| $N_{exp} = 3$ fits to | 3/24 | 1 | 0.135(2) | -0.0105(8) | |
| (1,loc) and (2,loc) | | 2 | 0.028(6) | 0.100(8) | |
| | | 3 | 0.030(9) | 0.045(12) | |
| $N_{exp} = 3$ fits to | 7/24 | 1 | 0.135(3) | -0.0104(8) | -0.0023(4) |
| (1,loc), (2,loc) | | 2 | 0.02(4) | 0.14(8) | -0.01(3) |
| and (3,loc) | | 3 | 0.01(6) | -0.04(9) | 0.11(2) |

lated propagators for mesons, $A$ and $B$, having different quantum numbers. We call them the "ratio" method and the "correlated-$\delta E$" method.

In the ratio method we take our 840 measurements for each meson $A$ and $B$ and create a jackknife ensemble of ratios of correlations. This is then fit to a single exponential to determine $\delta E$. In the correlated-$\delta E$ method we pick a set of correlations for each meson and fit the two sets simultaneously using

$$G_{\text{meson } A}(n_{sc}, \text{loc}; t) = \sum_{k=1}^{N_{exp}} c_A(n_{sc}, k) e^{-E_k^A \cdot t},$$

$$G_{\text{meson } B}(n_{sc}, \text{loc}; t) = c_B(n_{sc}, 1) e^{-(E_1^A + \delta E) \cdot t}$$

$$+ \sum_{k=2}^{N_{exp}} c_B(n_{sc}, k) e^{-E_k^B \cdot t}. \quad (20)$$

Of the two methods the second is more general, since it is straightforward to include higher exponentials and handle spin splittings of excited states. We have estimated the effects of higher states on the ratio method by fitting the jackknifed ratio ensemble to

$$R(t) = A_1 e^{-\delta E \cdot t} \frac{1 + A_2 e^{-\delta E_2 \cdot t}}{1 + A_3 e^{-\delta E_2 \cdot t}}. \quad (21)$$

We did not find a signal for the correction terms and the value for $\delta E$ was consistent with those from naive one-exponential fits only with slightly larger errors. We give examples of fits to the $\Upsilon$-$\eta_b$ splitting and one of the $\chi_b$ splittings in Tables VII and VIII. For the ratio method we use (1,loc) correlations and for the correlated-$\delta E$ method (1,loc) and (2,loc) correlations for each meson. We see that it is possible to get $\Upsilon$-$\eta_b$ splittings with 0.5 MeV and $\chi_b$ splittings with 5–10 MeV statistical errors (again using $a^{-1}$ of 2.4 GeV).

### C. Fit results

Using the fitting procedures of the previous subsections we obtained energies for the $\Upsilon$, $\Upsilon'$, $\Upsilon''$ levels, the $h_b$, $h_b'$ levels, the $\Upsilon$-$\eta_b$ splitting and for the splittings between the $\chi_b$ levels. For $aM_b^0 = 1.71$ we also have results for $D$ states (to date we have only looked at averages over the five polarizations of the $^1D_2$ state and leave more detailed studies of $D$-state fine structure and mixing with $S$ states to future work). Our estimates for the energies and splittings in dimensionless units are shown in Table IX for several $M_b^0$ values. For comparison we also show results for data without relativistic and finite lattice spacing corrections ($\delta H = 0$) and for another set of data without tadpole improvement ($u_0 = 1$). The errors in Table IX differ slightly from the purely statistical errors of previous tables. In those tables one saw that the cen-

TABLE VI. Examples of fits to $^1P_1$ correlations.

| | $N_{exp}$ | $t_{min}/t_{max}$ | $aE_1$ | $aE_2$ | $Q$ |
|---|---|---|---|---|---|
| 2 × 2 matrix | 2 | 8/24 | 0.630(4) | 0.82(3) | 0.15 |
| fits | | 7/24 | 0.630(3) | 0.81(2) | 0.17 |
| | | 6/24 | 0.632(5) | 0.84(1) | 0.03 |
| | | 8/14 | 0.625(5) | 0.83(1) | 0.19 |
| | | 7/14 | 0.626(4) | 0.80(2) | 0.22 |
| Fits to (1,loc) | 2 | 8/24 | 0.630(6) | 0.85(3) | 0.008 |
| and (2,loc) | | 7/24 | 0.628(5) | 0.82(2) | 0.008 |
| | | 8/14 | 0.628(10) | 0.82(3) | 0.23 |
| | | 7/14 | 0.626(8) | 0.81(2) | 0.35 |
| | 3 | 7/14 | 0.629(16) | 0.88(19) | 0.22 |
| | | 4/14 | 0.626(9) | 0.79(6) | 0.40 |

TABLE VII. $^1S_0$-$^3S_1$ splitting.

| | $N_{exp}$ | $t_{min}/t_{max}$ | $a\delta E$ | $Q$ |
|---|---|---|---|---|
| Ratio Method | 1 | 18/24 | 0.0123(2) | 0.21 |
| | 1 | 16/24 | 0.0123(2) | 0.21 |
| | 1 | 12/24 | 0.0126(2) | 0.09 |
| | 1 | 8/24 | 0.0129(1) | 0.005 |
| Correlated | 2 | 8/24 | 0.0123(2) | 0.39 |
| $\delta E$ fits | 2 | 7/24 | 0.0123(2) | 0.49 |
| | 2 | 6/24 | 0.0122(2) | 0.48 |

TABLE VIII. Example of $P$-state fine structure: $^3P_2$-$^3P_0$ splitting.

| | $N_{exp}$ | $t_{min}/t_{max}$ | $a\delta E$ | $Q$ |
|---|---|---|---|---|
| Ratio Method | 1 | 10/24 | 0.021(4) | 0.77 |
| | 1 | 9/24 | 0.020(4) | 0.79 |
| | 1 | 8/24 | 0.017(3) | 0.70 |
| | 1 | 7/24 | 0.016(2) | 0.76 |
| | 1 | 6/24 | 0.017(2) | 0.77 |
| Correlated | 2 | 8/24 | 0.023(7) | 0.52 |
| $\delta E$ fits | 2 | 7/24 | 0.021(6) | 0.55 |
| | 2 | 6/24 | 0.018(5) | 0.64 |

tral values and statistical errors depend sometimes on the fitting procedure used (and on $t_{min}/t_{max}$), and we have tried to take that into account in Table IX. Only fits with good $Q$ values ( $Q \geq 0.2$ ) and effective amplitude plots were included in these considerations. The reader may want to compare earlier tables with the $aM_b^0 = 1.71$ column in Table IX.

There are several features worth noting in Table IX. For instance, the splittings between $1\,^3S_1$ and $1\,^1P_1$ (spin-averaged $P$ state) as well as between $2\,^3S_1$ and $1\,^3S_1$ levels are insensitive to $M_b^0$ within errors. This is known to hold in the real world when one compares splittings in the $J/\psi$ and $Υ$ systems. Also, for spin-averaged quantities the $\delta H = 0$ results are almost indistinguishable from results with higher order corrections, except maybe for a slight lowering of the $1S$ level. Considering next the spin dependent splittings, one sees that the $^3S_1$-$^1S_0$ splitting does depend on $M_b^0$, as expected. More striking is the sensitivity of spin splittings to tadpole-improvement. The splittings are reduced by a factor of $\sim \frac{1}{2}$ without tadpole-improvement (i.e. if $u_0 = 1$). As we shall see, the tadpole-improved results agree well with experiment. Tadpole-improvement of the lattice action appears crucial if one wants to work with tree-level values $c_i = 1$. Otherwise spin splittings are badly underestimated.

## IV. COMPARISONS WITH EXPERIMENT

To compare our results with experiment we must convert from dimensionless lattice units to physical units by setting the scale $a^{-1}$. Before doing so, it is worthwhile reminding ourselves of systematic errors still contained in our simulations. The largest source of systematic errors, we believe, comes from the quenched approximation. One expects, among other things, corrections to both the $1S$-$1P$ and the $1S$-$2S$ splittings, and inverse lattice spacings obtained by fitting these splittings to experimental data should differ from each other. For instance, a bootstrap estimate for the ratio of splittings, $[E(2\,^3S_1) - E(1\,^3S_1)]/[E(1\,^1P_1) - E(1\,^3S_1)] \equiv R$, gives $R = 1.41(7)$ for $aM_b^0 = 1.71$; $R = 1.38(8)$ for $aM_b^0 = 1.8$; and $R = 1.35(8)$ for $aM_b^0 = 2.0$. The experimental value for this ratio is $R_{expt} = 1.28$, and one sees a possible 1 to 2 $\sigma$ deviation in our simulations. Inverse lattice spacings obtained from matching the $S$-$P$ splitting to experiment will differ from that obtained using the $1S$-$2S$ splittings by 1 or 2 $\sigma$. Taking splittings from Table IX that is indeed what we find. Work is underway to repeat simulations of the $Υ$ system with unquenched gauge configurations. It will be interesting to see how the ratio of splittings will shift. From potential models one can argue that the $1S$-$1P$ splitting will suffer a larger change than the $1S$-$2S$ splitting, and that the ratio $R$ defined above will decrease as one goes from the quenched to unquenched world. The other two major sources of systematic error in our calculation are fitting errors and the finite lattice spacing and relativistic errors in the NRQCD propagators. Our experience with fitting indicates that the results tend to move around by about a standard deviation when different methods are used, in other words the systematic fitting errors are probably about the same size as the statistical errors, while we expect systematic errors in the propagators to contribute at the 5 MeV level to the spectrum.

In order to present dimensionful results we need to define one global ( or "average") $a^{-1}$. We do so by calculating a bootstrap average based on the $1S$-$2S$ and $1S$-$1P$ splittings. The results are shown in Table X. There we give $a^{-1}$'s, separately for the two splittings plus the bootstrap values for averages and differences. We show results for two different ensembles for the $P$ states, the first obtained using smeared-local fits and the second based on matrix fits (see Table VI for spread in results due to fitting procedure dependence). We use the bootstrap average plus its associated error to define a global $a^{-1}$:

TABLE IX. Fit results for dimensionless energies and splittings, $aE$ and $a\delta E$.

| | $aM_b^0 = 1.71$ | 1.8 | 2.0 | 1.8 ($\delta H = 0$) | 1.8 ($u_0 = 1$) |
|---|---|---|---|---|---|
| $1\,^3S_1$ | 0.4534(8) | 0.4505(10) | 0.444(1) | 0.448(1) | 1.097(1) |
| $2\,^3S_1$ | 0.695(10) | 0.69(1) | 0.68(1) | 0.69(1) | 1.335(8) |
| $3\,^3S_1$ | 0.82(5) | 0.83(4) | 0.83(5) | 0.84(5) | 1.48(3) |
| $1\,^1P_1$ | 0.626(8) | 0.627(12) | 0.619(10) | 0.634(13) | 1.27(1) |
| $2\,^1P_1$ | 0.81(3) | 0.80(4) | 0.79(4) | 0.81(4) | 1.43(3) |
| $1\,^1D_2$ | 0.76(3) | | | | |
| Splittings: | | | | | |
| $^3S_1 - {}^1S_0$ | 0.0123(2) | 0.0116(2) | 0.0106(2) | | 0.0049(1) |
| $^3P_2 - {}^3P_0$ | 0.020(4) | 0.021(4) | 0.018(4) | | 0.011(3) |
| $^3P_2 - {}^3P_1$ | 0.008(2) | 0.008(3) | 0.008(3) | | 0.0047(14) |

TABLE X. $a^{-1}$ from $1S$-$2S$ and $1S$-$1P$ splittings.

| $aM_b^0$ | From Table IX | | Bootstrap Results | | | |
|---|---|---|---|---|---|---|
| | $a^{-1}(1S\text{-}2S)$ | $a^{-1}(1S\text{-}1P)$ | $a^{-1}(1S\text{-}2S)$ | $a^{-1}(1S\text{-}1P)$ | Average $a^{-1}$ | $\Delta a^{-1}$ |
| 1.71 | 2.33(11) | 2.55(12) | 2.34(8) | 2.49(4) | 2.42(6) | 0.15(7) |
| | | | | 2.58(14) | 2.46(9) | 0.23(13) |
| 1.8 | 2.35(11) | 2.49(17) | 2.32(10) | 2.49(11) | 2.41(9) | 0.17(10) |
| | | | | 2.50(15) | 2.41(10) | 0.18(15) |
| 2.0 | 2.39(11) | 2.51(15) | 2.39(12) | 2.50(10) | 2.45(10) | 0.12(10) |
| | | | | 2.52(14) | 2.45(11) | 0.13(14) |

$$a^{-1} = 2.4(1) \text{ GeV}.$$

Using the central value $a^{-1} = 2.4$ GeV, one can convert Table IX into physical numbers. In Table XI we do that for $aM_b^0 = 1.71$ and compare with experiment. The agreement between simulation results and experiment is excellent, with most entries agreeing within $1\sigma$. It is hoped that once unquenched calculations are completed, lattice QCD results will follow experiment even more closely. Our experience with the present quenched calculations tells us that unquenching effects are small (this observation also follows from potential model calculations) and that high statistics data are required to see them. The entries in Table XI that do not have a corresponding experimental number attached are predictions of the theory. We predict $\Upsilon$ $D$ states with center of mass at $(10.20 \pm 0.07 \pm 0.03)$ GeV, where the second error comes from uncertainties in $a^{-1}$. Our current simulations give an $\eta_b$ state at $(9.431 \pm 0.005 \pm 0.001)$ GeV, where now the first (and dominant) error is due to higher-order relativistic and finite $a$ corrections not included in our action and the second error is due to $a^{-1}$. The $\eta_b$ energy is likely to change (decrease) when one goes beyond the quenched approximation. Given the small statistical errors on the $\eta_b$ - $\Upsilon(1S)$ splitting this is one place where

TABLE XI. NRQCD spectrum results and comparison with experiment. We use $a^{-1} = 2.4$ GeV and $aM_b^0 = 1.71$. Systematic errors due to quenching, higher order terms in the NRQCD action and uncertainty in the scale $a^{-1}$ are not included.

| | Simulation Results [GeV] | Experiment [GeV] |
|---|---|---|
| $2^3S_1$-$1^3S_1$ | 0.580(26) | 0.563 |
| $3^3S_1$-$1^3S_1$ | 0.88(12) | 0.895 |
| $1^1P_1$-$1^3S_1$ | 0.414(22) | 0.440 |
| $2^1P_1$-$1^3S_1$ | 0.86(7) | 0.800 |
| $1^1D_2$-$1^3S_1$ | 0.74(7) | |
| $^3S_1$-$^1S_0$ | 0.0295(5) | |
| $^3P_2$-$^3P_0$ | 0.048(10) | 0.053 |
| $^3P_2$-$^3P_1$ | 0.019(5) | 0.021 |
| $^3P_{CM}$-$^1P_1$ | 0.005(1) | |

effects of quenching could be observable.

The spectrum results are shown in Figs. 1 and 2 of Sec. I. The $P$-state fine structure is measured relative to the center of mass of the triplet states. We first create bootstrap ensembles of individual $P$-state energies. We then calculate bootstrap estimates for the center of mass and for energies relative to the center of mass. In Fig. 2 the energy of the $^1P_1$ state (the $h_b$) lies slightly below the triplet center of mass. We note, however, that within our $\sim 5$ MeV systematic errors the two levels are consistent with each other.

One quantity of phenomenological interest is the mesonic wave function at the origin (i.e., zero separation between quark and antiquark), which for the $\Upsilon(mS)$ is

$$\Psi_m(0) = \left\langle m \left| \sum_{\mathbf{x}} \psi^\dagger(\mathbf{x})\, \sigma_z\, \chi^\dagger(\mathbf{x}) \right| 0 \right\rangle,$$

$$= \langle m | \text{loc} \rangle_{^3S_1 z} \tag{22}$$

where $|0\rangle$ is the fock space vacuum, $\langle m|$ is the quantum state of an $\Upsilon(mS)$ polarized in the $z$ direction, and $|\text{loc}\rangle_{^3S_1 z}$ is the state created by our loc smearing function in the $^3S_1 z$ channel. Examining Eq. (18), we see that (in the limit of an infinite number of exponentials in our fit ansatz) $\langle m|\text{loc}\rangle_{^3S_1 z}$ measured in units of $a^{-3/2}$ is just the fit parameter $a(\text{loc}, m)$, which in turn is equal to $\sqrt{b(\text{loc}, m)}$. We extract $b(\text{loc}, m)$ by fitting simultaneously to $G_{^3S_1}(\text{loc}, \text{loc}; t)$, $G_{^3S_1}(1, \text{loc}; t)$, $G_{^3S_1}(2, \text{loc}; t)$, and $G_{^3S_1}(3, \text{loc}; t)$. These are fits of the same form as Eq. (19), but including $n_{sc} = \text{loc}$. In addition to obtaining $a^{3/2}\langle m|\text{loc}\rangle$ directly from our fits, it can be obtained indirectly from our separate fits to $a$ and $b$.

$$a^{3/2}\, \Psi_m(0) = \frac{b(n_{sc}, m)}{a(n_{sc}, m)} = a^{3/2}\, \frac{\langle n_{sc}|m\rangle\, \langle m|\text{loc}\rangle}{\langle n_{sc}|m\rangle}, \tag{23}$$

for any initial smearing function $n_{sc}$. In Table XII we have tabulated measurements of $a^{3/2}\, \Psi_m(0)$, from direct fits to $b(\text{loc}, m)$ and from ratios of $b(n_{sc}, m)$ and $a(n_{sc}, m)$

TABLE XII. Mesonic wave function at the origin, $a^{3/2} \Psi(0)$. A dashed line means that no signal could be extracted.

| Meson (mS) | Direct Fit to $b(\mathrm{loc}, m)$ | Using $b(n_{sc}, m)/a(n_{sc}, m)$ | | |
|---|---|---|---|---|
| | | $n_{sc} = 1$ | $n_{sc} = 2$ | $n_{sc} = 3$ |
| $\Upsilon(1S)$ | 0.153(2) | 0.154(2) | 0.162(12) | 0.17(2) |
| $\Upsilon(2S)$ | 0.147(10) | 0.16(3) | 0.127(10) | — — — — |
| $\Upsilon(3S)$ | — — — — | 0.32(10) | — — — — | 0.14(4) |
| $\eta_b(1S)$ | 0.161(2) | 0.162(2) | 0.184(26) | — — — — |
| $\eta_b(2S)$ | 0.147(9) | 0.17(4) | 0.132(10) | — — — — |
| $\eta_b(3S)$ | — — — — | — — — — | — — — — | 0.13(2) |

taken from Table IV and Table V. We also present results for $\eta_b$. For ground states, values obtained using different initial smearing functions are consistent. In general, we believe the diagonal entries in Table XII with $n_{sc} = m$ are the most reliable. Good smearing functions imply that off-diagonal amplitudes are severely suppressed. Signal to noise for the off-diagonal amplitudes $a(n, m)$ and $b(n, m)$ and for their ratios is not as good as for the diagonal amplitudes. The "direct fit" estimates for $\Psi(0)$ suffer from the fact that $b(\mathrm{loc}, m)$ comes from fitting the local-local meson correlation function. This correlation has many more exponentials contributing out to large $t$ values than is the case for smeared-local correlations (this is the reason why the local-local correlation was not used in any of our fits to extract energies). Hence, it has proven difficult to extract the amplitude for any given excited state accurately using the local-local correlation. The indirect method of Eq. (23) gets around this problem and uses only smeared-local and smeared-smeared correlations.

Care should be used in any attempt to relate these values of the wave function to predictions of physical processes, such as the leptonic width of the $\Upsilon$. A complete calculation of such processes will involve large (10–20 % or more) corrections in relating the lattice current appearing in Eq. (22) to continuum currents. These corrections arise both from relativistic (coming from the small components of the heavy Dirac spinors) and renormalization effects. In addition, $|\Psi(0)|^2$ scales like $a^{-3}$; meaning that lattice spacing errors in the dimensionful value of $|\Psi(0)|^2$ will be of order 13%. Quenching effects are likely to induce an additional systematic error on the simulation results, which we have not attempted to estimate quantitatively. If one nonetheless goes ahead and combines the numbers in Table XII with $a^{-1} = 2.4(1)$ GeV and with the standard leading order Van Royen-Weisskopf formula for a vector meson leptonic width [14], one finds for the $\Upsilon(1S)$, $\Gamma_{ee} = (1.09 \pm 0.03 \pm 0.14)$keV. The experimental value is $\Gamma_{ee}^{(\mathrm{expt})}(\Upsilon) = (1.34 \pm 0.04)$keV. In the simulation result we only quote two errors corresponding respectively to statistical errors and $a^{-1}$ uncertainties. Quenching errors and relativistic and matching corrections (corrections that are expected to dominate) have not been included. Unquenching should increase the theoretical estimate for $\Gamma_{ee}$ by enhancing $|\Psi(0)|^2$. Using the diagonal entries in Table XII, one finds for the $\Upsilon$ 2S and 3S, $\Gamma_{ee}(2S) = (0.66 \pm 0.10 \pm 0.09)$keV

and $\Gamma_{ee}(3S) = (0.75 \pm 0.37 \pm 0.10)$keV. The experimental numbers are respectively (using the $\mu^+\mu^-$ branching ratios), $\Gamma_{ee}^{(\mathrm{expt})}(2S) = (0.56 \pm 0.09)$keV and $\Gamma_{ee}^{(\mathrm{expt})}(3S) = (0.44 \pm 0.04)$keV. When one compares $\Psi(0)$ given in Table XII for the ground and excited states one finds that the ratios $\Psi_{2S}(0)/\Psi_{1S}(0)$ and $\Psi_{3S}(0)/\Psi_{1S}(0)$ are larger than one would expect from lattice potential calculations. Our excited state leptonic widths lie above the experimental numbers (although consistent within large errors), whereas for $\Upsilon(1S)$ the simulation result lies below experiment. Once corrections to the present calculation are included (e.g., relativistic, quantum loop, lattice-continuum matching, unquenching), it will be important to monitor and understand how and whether these discrepancies go away. At the same time, one also needs to reduce the statistical errors, particularly for the excited states. We hope to be reporting on more accurate results in the future.

## V. Υ MASS AND LORENTZ INVARIANCE

As we have shown, NRQCD simulations give accurate results for the splittings between $b\bar{b}$ states. These simulations can also be used to compute the full mass of the $\Upsilon$. We use the $\Upsilon$ mass to determine the correct quark mass for the simulation. We have investigated two different methods for computing the $\Upsilon$ mass.

The first method is to add twice the renormalized mass of the quark to the nonrelativistic energy $E_{\mathrm{NR}}(\Upsilon)$ obtained from the simulation:

$$M_\Upsilon = 2(Z_m M_b^0 - E_0) + E_{\mathrm{NR}}(\Upsilon). \tag{24}$$

Here $Z_m$ and $E_0$ are renormalizations that are computed using perturbation theory [5,15]. Our results are shown in Table XIII. The uncertainties in this procedure are due to uncalculated $O(\alpha_s^2)$ corrections in the perturbative expansions of the renormalizations, and to uncertainties in $a^{-1}$.

The second method is to compute the nonrelativistic energy for $\Upsilon$'s with nonzero three momenta. We did this for momenta $\mathbf{p} = (0,0,1)$, $(0,1,1)$, $(1,1,1)$, and $(0,0,2)$ in units of $4\pi/16a$, and fit the resulting energies to two different parametrizations:

$$E_\Upsilon(\mathbf{p}) - E_{\mathrm{NR}}(\Upsilon) = \frac{\mathbf{p}^2}{2 M_{\mathrm{kin}}} - C_1 \frac{(\mathbf{p}^2)^2}{8 M_{\mathrm{kin}}^3} \tag{25}$$

TABLE XIII. The $\Upsilon$ mass as determined from the $\Upsilon$'s non-relativistic rest energy in NRQCD. The last column assumes $a^{-1} = 2.4(1)$.

| $aM_b^0$ | $a\,E_{\mathrm{NR}}$ | $Z_m$ | $a\,E_0$ | $a\,M_\Upsilon$ | $M_\Upsilon$ (GeV) |
|---|---|---|---|---|---|
| 1.71 | 0.453(1) | 1.20(4) | 0.32(6) | 3.92(18) | 9.4(6) |
| 1.8 | 0.451(1) | 1.18(4) | 0.31(6) | 4.08(18) | 9.8(6) |
| 2.0 | 0.444(1) | 1.16(3) | 0.30(6) | 4.48(17) | 10.8(6) |

and

$$E_\Upsilon(\mathbf{p}) - E_{\mathrm{NR}}(\Upsilon) = \frac{\mathbf{p}^2}{2\,M_{\mathrm{kin}}}$$

$$-\frac{1}{8M_{\mathrm{kin}}^3}\left\{ (\mathbf{p}^2)^2 + C_2 \sum_{k=1,2,3} p_k^4 \right\}.$$

$$(26)$$

In a Lorentz invariant theory, the kinetic mass $M_{\mathrm{kin}}$ is equal to the rest mass of the upsilon; in our simulations this should be true up to corrections of order $v^4$, except in the $\delta H = 0$ theory where the errors should be order $v^2$. The $(\mathbf{p}^2)^2$ terms in our fits test for higher-order relativistic effects; we expect $C_1 = 1$ up to corrections of order $O(v^2, a^2)$, except in the $\delta H = 0$ theory where this parameter should almost vanish. The $p_k^4$ term in the second fit tests for contributions that are not rotationally invariant; we expect $C_2 = 0$ up to corrections of $O(v^2, a^2)$. These expectations are confirmed by our results which are shown in Table XIV.

Our two methods give identical $\Upsilon$ masses in lattice units to better than 1%. Assuming $a^{-1} = 2.4(1)$, our results indicate that the correct bare mass for a $b$ quark is $M_b^0 = 1.7(1)/a$; among our simulations, the set with $a\,M_b^0 = 1.71$ is the best.

The close agreement between our two determinations is striking confirmation of the partial restoration of Lorentz invariance due to the correction terms $\delta H$ that we include in the quark evolution equation. The kinetic mass is quite sensitive to these correction terms; it is too small by almost 10% when we set $\delta H = 0$. This is what we expect since $M_{\mathrm{kin}}$ equals twice the quark mass in a nonrelativistic theory, while in a relativistic theory the binding energy contributes as well. Note that tadpole improvement is also essential; without it, $M_{\mathrm{kin}}$ is too large by almost 25%.

Each of the two methods we use to determine the $\Upsilon$ mass has its strengths and weaknesses. Using $M_{\mathrm{kin}}$ is attractive because there is no need for perturbative calculations, but it is only accurate if the $\delta H$ correction terms are included in the quark propagators. The rest energy of the meson is quite insensitive to $\delta H$, but can only be used when combined with perturbative results for the quark mass renormalizations. Ideally one uses both methods and compares results, as we have done here.

## VI. SUMMARY

We have investigated the $\Upsilon$ system using nonrelativistic lattice QCD (NRQCD) and find that one can successfully reproduce the general features of the known $\Upsilon$ spectrum, including $P$-state fine structure and several excited states. We also make predictions for $D$ states and for $\eta_b$. By reducing the statistical errors in the splittings by a modest amount, one should, in the future, be able to study effects of quenching in a quantitative way.

We worked with an action correct through $O(M_b\,v^4)$ and whose link variables had been divided by $u_0$, the fourth root of the plaquette value, i.e., with a tadpole-improved action. Because of tadpole improvement we were able to get good results (e.g., the correct $P$-state fine structure splittings) with tree-level coefficients for the correction terms in the NRQCD action. Our program should be viewed as a demonstration of a successful

TABLE XIV. The $\Upsilon$ mass determined from its kinetic mass $M_{\mathrm{kin}}$ using two different fits. The parameters $C_1$ and $C_2$ are explained in the text. The last column assumes $a^{-1} = 2.4(1)$.

| $aM_b^0$ | $aM_{\mathrm{kin}}$ | $C_1$ | $C_2$ | $Q$ | $M_{\mathrm{kin}}$ (GeV) |
|---|---|---|---|---|---|
| 1.71 | 3.94(3) | 1.0(3) | | 0.16 | 9.5(4) |
| | 3.94(3) | | 0.20(37) | 0.19 | |
| 1.8 | 4.09(3) | 1.1(3) | | 0.60 | 9.8(4) |
| | 4.09(3) | | 0.20(35) | 0.62 | |
| 2.0 | 4.48(4) | 1.2(3) | | 0.64 | 10.8(4) |
| | 4.48(4) | | 0.24(36) | 0.67 | |
| 1.8 | 3.82(3) | 0.23(32) | | 0.06 | 9.2(4) |
| ($\delta H = 0$) | 3.83(3) | | -0.45(41) | 0.006 | |
| 1.8 | 4.96(3) | 1.4(3) | | 0.11 | |
| ($u_0 = 1$) | 4.97(3) | | 0.60(35) | 0.18 | |

implementation of perturbative improvement of a lattice action. Our results underscore the utility of tree-level improvement and the crucial importance of tadpole improvement.

We have put considerable effort into developing fitting procedures that allow us to get not just ground state energies and energy splittings between levels with different quantum numbers, but also (radially) excited energy levels. We find that it is important to fit several correlations simultaneously, and do multiexponential multicorrelation fits.

Our calculations have systematic errors at the 5 MeV level coming from higher-order relativistic and finite lattice spacing effects. The largest source of uncertainty comes, however, from the quenched approximation. Calculations involving dynamical configurations are under-

way, and we will be reporting on them soon. Quenched $c\bar{c}$ spectrum results will also appear shortly.

## ACKNOWLEDGMENTS

[1] For recent reviews see articles by C. W. Bernard and by R. D. Kenway, in *Lattice '93*, Proceedings of the International Symposium, Dallas, Texas, edited by T. Draper *et al.* [Nucl. Phys. B (Proc. Suppl.) **34** (1994)].

[2] A. El-Khadra, G. Hockney, A. Kronfeld, and P. Mackenzie, Phys. Rev. Lett. **69**, 729 (1992); A. El-Khadra, in *Lattice '93* [1], p. 141.

[3] G. P. Lepage and J. Sloan, *Lattice '93* [1], p. 417; C. T. H. Davies, *ibid.*, p. 135; G. P. Lepage, *Lattice QCD for Small Computers*, lectures presented at TASI 93 and at the UK Summer Institute; C. T. H. Davies *et al.*, Cornell Report No. CLNS 94/1296 (unpublished).

[4] For other lattice determinations of $\alpha_s$ see M. Luescher, R. Sommer, P. Weisz, and U. Wolff, Nucl. Phys. **B413**, 481 (1994); U. Wolff, in *Lattice '93* [1], p. 243; K. Schilling and G. S. Bali, *ibid.*, p. 147.

[5] C.T.H. Davies *et al.*, Phys. Rev. Lett. **73**, 2654 (1994).

[6] G. P. Lepage and B. A. Thacker, in *Field Theory on the Lattice*, Proceedings of the International Symposium, Seillac, France, 1987, edited by A. Billoire *et al.* [Nucl. Phys. B (Proc. Suppl.) **4**, 199 (1988)]; B. A. Thacker and G. P. Lepage, Phys. Rev. D **43**, 196 (1991).

[7] G. P. Lepage, L. Magnea, C. Nakhleh, U. Magnea, and K. Hornbostel, Phys. Rev. D **46**, 4052 (1992).

[8] K. Symanzik, Nucl. Phys. **B226**, 187 (1983); **B226**, 205 (1983).

[9] S. Hashimoto, Nucl. Phys. B (Proc. Suppl.) **34**, 441 (1994); Phys. Rev. D **50**, 4639 (1994); UKQCD Collaboration, poster session given at *Lattice '93* by C. T. H. Davies, Nucl. Phys. B (Proc. Suppl.) **34**, 437 (1994).

[10] C. T. H. Davies and B. A. Thacker, Nucl. Phys. **B405**, 593 (1993); S. M. Catterall, F. R. Devlin, I. T. Drummond, and R. R. Horgan, Phys. Lett. B **321**, 246 (1994).

[11] G. P. Lepage and P. B. Mackenzie, Phys. Rev. D **48**, 2250 (1993).

[12] The Υ spectrum based on our $aM_b^0 = 1.8$ data was presented in [3]. We have now completed the analysis for several $aM_b^0$ values. The figures shown here are for $aM_b^0 = 1.71$, the value of $aM_b^0$ that gives the best absolute Υ($1S$) mass.

[13] M. Luescher and U. Wolff, Nucl. Phys. **B339**, 222 (1990).

[14] See for instance D. H. Perkins, *Introduction to High Energy Physics*, 3rd ed. (Addison-Wesley, Reading, MA).

[15] C. J. Morningstar, Phys. Rev. D **48**, 2265 (1993); Nucl. Phys. B (Proc. Suppl.) **34**, 425 (1994); Edinburgh Report. No. 94/1 (unpublished).